Mitochondrial Swelling Measurement In Situ by Optimized Spatial Filtering: Astrocyte-Neuron Differences

Akos A. Gerencser,*[†‡] Judit Doczi,* Beata Töröcsik,* Ella Bossy-Wetzel,[‡] and Vera Adam-Vizi*
*Department of Medical Biochemistry, Semmelweis University, Neurobiochemical Group, Hungarian Academy of Sciences, Szentagothai Knowledge Center, Budapest, Hungary; [†]Buck Institute for Age Research, Novato, California; and [‡]Apoptosis and Cell Death Program, Burnham Institute for Medical Research, La Jolla, California

ABSTRACT   Mitochondrial swelling is a hallmark of mitochondrial dysfunction, and is an indicator of the opening of the mitochondrial permeability transition pore. We introduce here a novel quantitative in situ single-cell assay of mitochondrial swelling based on standard wide-field or confocal fluorescence microscopy. This morphometric technique quantifies the relative diameter of mitochondria labeled by targeted fluorescent proteins. Fluorescence micrographs are spatial bandpass filtered transmitting either high or low spatial frequencies. Mitochondrial swelling is measured by the fluorescence intensity ratio of the high- to low-frequency filtered copy of the same image. We have termed this fraction the "thinness ratio". The filters are designed by numeric optimization for sensitivity. We characterized the thinness ratio technique by modeling microscopic image formation and by experimentation in cultured cortical neurons and astrocytes. The frequency domain image processing endows robustness and subresolution sensitivity to the thinness ratio technique, overcoming the limitations of shape measurement approaches. The thinness ratio proved to be highly sensitive to mitochondrial swelling, but insensitive to fission or fusion of mitochondria. We found that in situ astrocytic mitochondria swell upon short-term uncoupling or inhibition of oxidative phosphorylation, whereas such responses are absent in cultured cortical neurons.

INTRODUCTION

Mitochondrial swelling is a hallmark ultrastructural change occurring after in vivo brain ischemia (see (1)), and is one of the most important indicators of the opening of the mitochondrial permeability transition pore (2,3). In vitro assessment of mitochondrial swelling is widely performed in suspensions of isolated mitochondria by measuring light scatter. Most of our knowledge of brain mitochondrial swelling has been derived from observations in suspensions of isolated mitochondria containing both neuronal and astroglial mitochondria. In contrast, cell-type-specific differences between mitochondria are becoming recognized (4,5). Although mitochondrial swelling is an ultrastructural change, optical approaches are no less valuable than electron microscopy, because they allow detection of the temporal dynamics of mitochondrial swelling in living specimens. In situ fluorescence microscopic observations are often presented without quantification (6). Quantification of morphological changes of mitochondria has been done by manual scoring (7) or by calculation of rounding up of mitochondria in binarized and segmented images (8). In situ mitochondrial swelling has been quantified by isosurface measurement in deconvolved image stacks (9) or by angular light scatter using a modified transmitted-light microscope (10), a technique that is also dependent on a specialized optical design. Quantitative techniques used so far have been strongly hindered by the dynamic behavior of mitochondria: fusion and fission, motion, and aggregation.

Mitochondria appear as punctate and filamentous details in fluorescence micrographs. Images can be composed by superposition of two-dimensional (2D) sine waves. The spatial frequency, or Fourier domain representation, of an image gives the amplitude and phase of individual sine wave components as a function of direction and spatial frequency. It is important to note that the punctate and filamentous details are represented at high spatial frequencies. Previously we separated the mitochondrial fluorescence from the background fluorescence of a calcium probe with imperfect mitochondrion selectivity by spatial filtering with high-pass characteristics (11). The spatial filtering was performed in Fourier domain, passing the high-spatial-frequency components corresponding to punctate and filamentous image details while rejecting the bulky, diffuse features. In contrast, bandpass filtering gives information about the amplitude of a given frequency range (band), or, in fluorescent images, yields the intensity of puncti and filaments with a given range of diameters. Therefore, the relative contribution of fluorescence intensities of thinner and thicker punctate or filamentous structures to the complete image can be measured by using a set of two bandpass spatial filters. Based on the ratio calculation of the amount of fluorescence of thin structures to that of thicker structures, we describe a novel morphometric technique here, termed the thinness ratio (TR), or ratiometric optimized spatial filtering technique. We use the TR technique as a sensitive assay of diameter changes of in situ mitochondria. The output of the technique is determined by

the characteristics of the two bandpass spatial filters. These filters are generated by a numerical optimization algorithm to maximize the sensitivity of the technique for artificially induced mitochondrial swelling depicted by a calibration image series. The TR technique is remarkable in that it uses spatial frequency components smaller than the diffraction-limited bandwidth of optical microscopy, and therefore the diameter estimates are not limited by the resolution of light microscopy. The Fourier domain image processing also overcomes the limitations of the detector resolution.

Besides validation and characterization of the TR technique, this article shows remarkable differences between astrocytic and neuronal mitochondria. Mitochondrial swelling is a typical response of cortical astrocytes for short-term uncoupling or inhibition of oxidative phosphorylation. In contrast, neuronal mitochondria do not swell in these conditions.

MATERIALS AND METHODS

Materials

pDsRed2-mito (mito-DsRed2) was purchased from Clontech (Mountain View, CA). The mitochondrially targeted redox sensitive GFP1 (mito-roGFP1) was a gift of Dr. James Remington (12). Mastoparan was purchased from Calbiochem (EMD, San Diego, CA). All other reagents were obtained from Sigma or Fluka (St. Louis, MO) unless otherwise stated.

Cell cultures and transfections

Primary cultures of cortical astrocytes were prepared from P0-1 Wistar rat pups, plated on poly-L-ornithine-coated 12-mm coverslips and cultured in DMEM supplemented with 10% fetal bovine serum for 10-13 days at 37°C, 5% CO_2. Primary neuron-enriched cultures were prepared from E17 Wistar rat embryos, plated on 6 mm glass coverslips coated with poly-L-ornithine plus laminin in 12-well plates and maintained in Neurobasal medium (Invitrogen, Carlsbad, CA) supplemented with 2% B27 supplement (Invitrogen) and 2 mM glutamine for 8–12 days at 37°C, 5% CO_2. Mixed cortical cultures were prepared from rat cortices (BrainBits LLC, Springfield, IL) and cultured in poly-D-lysine-coated Lab-Tek I 8-well chambered coverglasses (Nunc, Rochester, NY) at a density of 10^5 cells/well in Neurobasal medium containing 2% B27 supplement, 2 mM GlutaMAX, 2% fetal bovine serum, and 100 IU/ml penicillin plus 100 μg/ml streptomycin. Cultures were transfected at 7–9 days (for neuron-enriched and mixed cultures) or at 12–14 days in culture (for astrocytes) using Lipofectamine 2000 (Invitrogen) in Neurobasal medium at a 3:2 ratio of Lipofectamine (μl) to plasmid DNA (μg); 3 μg and 0.2 μg of DNA was transfected per well of 12-well and Lab-Tek plates, respectively. Experiments were carried out at days 1 and 3–4 posttransfection for mito-DsRed2 and mito-roGFP1, respectively. Typical transfection rates were low (<1%), and visualized individual, nonoverlapping cells.

Mitochondrial isolation and light-scatter measurements

Rat brain mitochondria were isolated on a Percoll gradient from cortices of adult Wistar rats as described by Chinopoulos et al. (13). Mitochondrial swelling was measured with a GBC UV/VIS 920 spectrophotometer that measured absorbance at 540 nm in a medium (13) containing mitochondria (0.25 mg/ml) and (in mM) 125 KCl, 20 HEPES, 2 KH_2PO_4, 0.025 EGTA, 4 $MgCl_2$, 0.2 ATP, 5 malate, and 5 glutamate, pH 7.08 (titrated with KOH), 37°C.

Imaging

Time-lapse fluorescence microscopy was carried out at 37°C at continuous superfusion for astrocyte and neuron-enriched cultures, and without super-fusion for mixed cortical cultures, in a medium containing (in mM) 150 NaCl, 5.4 KCl, 1.8 $CaCl_2$, 1 $MgCl_2$, 0.9 NaH_2PO_4, 20 HEPES, and 5.6 glucose at pH 7.4. Experiments on primary astrocytes (see Fig. 5) were performed as single-plane wide-field imaging on a Nikon Diaphot 200 inverted microscope (Plan Fluor 100× 1.3 NA) equipped with a 75-W xenon arc lamp (Polychrome II, Till, Munich, Germany) plus an additional 535/20 nm exciter, 560LP dichroic mirror, and 570LP emitter (Omega Optical, Brattleboro, VT). Image series of 512 × 512 pixel frames (12 bit; 2- to 5-s acquisition interval, no binning, 500 ms exposure time, using a 4× projection lens yielding ~0.1 μm pixel size) were acquired using a Micromax cooled digital CCD camera (Princeton Instruments, Trenton, NJ) under control of MetaFluor 3.5 software (Molecular Devices, Downingtown, PA).

Experiments in primary neuron-enriched cultures (see Fig. 8) were performed on a Zeiss LSM-510 laser scanning confocal microscope with a Plan-Neofluar 40 × 1.3 NA lens and recording five to six planes of 512 × 512 pixel frames (12-bit; 0.075 × 0.075 × 1 μm^3 voxel size), at 25 sec acquisition interval, at 1.2 Airy unit (or resel; see below) pinhole, using the 543-nm line of a 5-mW HeNe laser at ≤7% power with an HFT 488/543 dichroic mirror and 560LP emission filter.

Experiments in mixed cortical cultures (see Fig. 10) were performed on an Olympus IX-81 inverted microscope equipped with a UAPO 40× oil 1.3 NA lens, 1.6× optovar, Lambda LS Xe-arc light source (175 W with ND 0.3), Lambda 10-2 excitation and emission filter wheels (Sutter Instruments, Novato, CA), a linear encoded xy-stage (Prior, Rockland, MA), and a Coolsnap HQ cooled digital CCD camera (Photometrics, Tucson, AZ; −30°C, 10 Mhz readout, high gain, 12-bit depth, 200 ms exposure time, recording a 512 × 512 pixel center square of the sensor at no binning, resulting in 0.1 μm pixel size). Z-stacks of seven planes with 0.8 μm spacing were recorded in 1-min intervals for three times at each measurement time point (at 0, 5, and 90 min). Mito-roGFP1 was imaged close to the isosbestic (redox-insensitive) excitation wavelength using a 438/24 nm excitation filter (Semrock, Rochester, NY) and 505LP dichroic mirror (74100, Chroma, Rockingham, VT) with 528/38 nm (Chroma) emission filter. The whole microscope stage was incubated at 37°C in atmospheric environment. Image acquisition was controlled by the Multidimensional acquisition application in Metamorph 6.3 (Molecular Devices). For astrocyte-neuron immunostaining α-MAP2 (mouse monoclonal, clone HM2 at 1:1000; Sigma) and α-GFAP (rabbit polyclonal at 1:1000; Dako, Carpinteria, CA) primary, and α-mouse-Alexa555 (1:250) and α-rabbit-Alexa594 (1:1000; donkey IgG, Invitrogen) secondary antibodies were used. Cultures were fixed and stained in the Lab-Tek chambers, and imaged in Prolong Gold DAPI antifade reagent (Invitrogen). Immunofluorescence was imaged in addition to mito-roGFP1 with the following filter sets (excitation-dichroic-emission, in nm): 555-560LP-588/21, 582/15-580LP-610LP, and 360-458LP-460/40.

Calculation of the TR

To obtain the TR, first, the original raw (or mean intensity z-projected stack) fluorescence image ($G(x,y)$; Fig. 1 A) was duplicated. Then, both images were spatially filtered (Eqs. 1 and 2), one by a high-spatial-frequency bandpass (HBP) and the other by a low-spatial-frequency bandpass (LBP) filter ($G'(x, y)$; Fig. 1, D and E, respectively). Finally, the TR was calculated as the ratio of the average fluorescence intensity in the HBP filtered image to that in the LBP filtered image (Eq. 3; where ⟨⟩ stands for region-of-interest mean). Spatial filtering was implemented as filtering in Fourier (frequency) domain and was performed as previously described (11). The spatial frequency (ω) is used technically in pixels corresponding to the Fourier domain image. One pixel of ω calibrates to one cycle per physical size of the image (μm).

$$G' = |\text{Re}(\text{F}^{-1}\{F\{G\} \cdot \hat{H}\})| \qquad (1)$$

$$\hat{H}(\omega_x, \omega_y) = f_{\text{filter}}(\omega) = f_{\text{filter}}\left(\sqrt{\omega_x^2 + \omega_y^2}\right) \qquad (2)$$

$$TR = \frac{\langle G'_{\text{high}}\rangle}{\langle G'_{\text{low}}\rangle} \qquad (3)$$

In Eqs.1 and 2 $\hat{H}(\omega_x, \omega_y)$ is the 2D transfer function of the spatial filter (ω_x and ω_y stand for coordinates in spatial frequency, considering the origin in the center of the quadrangular image) and F{} stands for discrete Fourier transformation. $f_{\text{filter}}(\omega)$ is the scalar filter function (defined in Eq. 4), which determines the shape of a slice of the 2D transfer function (Fig. 1, *B* and *C*). It is important to use the absolute value of the filtered image pixels in Eq. 1, because removal of lowest-frequency components yields zero mean at region of interest averaging. For the same reason, background removal is not required here. As filter functions Butterworth bandpass filters were used, calculated by the product of a low- and a high-pass filter function (Eq. 4):

$$f_{\text{filter}}(\omega) = \frac{1}{1 + \left(\dfrac{\omega_{\text{cuton}}}{\omega}\right)^{2\text{orderon}}} \frac{1}{1 + \left(\dfrac{\omega}{\omega_{\text{cutoff}}}\right)^{2\text{orderoff}}}. \qquad (4)$$

Each filter had four parameters: cuton and cutoff frequencies, and orders of cuton and cutoff functions. The two filters used for the TR determination total in eight parameters, however typically the same orders were used in all terms. Spatial filtering with narrow HBP filters often results in values too small for integer data storage. Therefore, $f_{\text{filter}}(\omega)$ was normalized by a k factor (Eq. 5):

$$k = \ln(1 + \omega_{\text{max}}) \bigg/ \int_0^{\omega_{\text{max}}} \frac{1}{1 + \omega} f_{\text{filter}}(\omega) d\omega. \qquad (5)$$

In Eq. 5, ω is given in pixels (ω_{max} is half of the image size in pixels $-$ 1). The k is 1 for $f_{\text{filter}}(\omega) = 1$ and increases for narrower and higher ω bandpass filters.

To amplify signals originating from highly fluorescent details of an image, a copy of the projected image was binarized according to the following

procedure. A copy of the duplicate was filtered with a minimum filter of window width 17 × 17 pixels and subtracted from the duplicate. The resultant image was gamma-corrected at $\gamma = 2$ and binarized at 0.9 times the optimal threshold value determined by Otsu's method (Mathematica; Digital Image Processing addon (14)). The bandpass-filtered images were multiplied by this mask image and the average fluorescence intensity was read out from regions of interest, not counting pixels of zero value. This was performed on all acquired data, but not on the model mitochondrion images, which did not contain background noise.

Calculation of TR images

TR images were calculated by dividing the pixel values of the HBP-filtered image with the corresponding pixel values of the LBP-filtered one, after running a maximum filter with a 7 × 7 window width on each image. The purpose of the maximum filtering was to eliminate the zero crossings of sine components, which were results of the bandpass filtering.

Optimization of the filter functions

The characteristics of the HBP and LBP filters determine what size details of the image are measured by the TR. The filter characteristics are given by the coefficients of Eq. 4. To obtain the best parameters for a given application we optimized parameters using two sets of images: a set of baseline images (frames of a time lapse of one cell) and a set of images after treatment (the same cell with swollen mitochondria). Optimization was done by comparing the results of the TR calculation between the two sets of images using Student's *t*-test. The parameters were optimized by finding the minimum of the *p*-values (Fig. 2 *A*). This was done by numerical global optimization using differential evolution (15) in the NMinimize standard function of Mathematica 5.2 (Wolfram Research, Champaign, IL) or in a custom developed Pascal language software (the latter was used for the results shown). Fig. 2 *E* indicates that there are favored filter parameters with (local) minimum of the *p*-values. The optimization was performed on five parameters on constrained
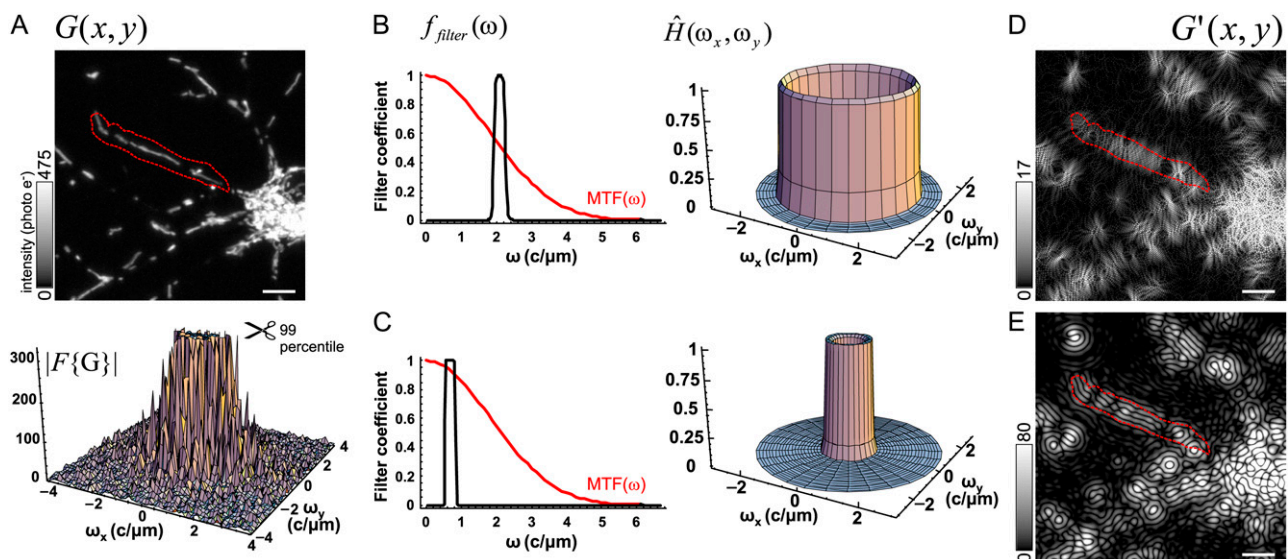

FIGURE 1 Computation of the thinness ratio. (*A*) Confocal maximum intensity projection image of a mito-DsRed2-expressing cortical neuron; original image ($G(x,y)$) and the absolute value of its discrete Fourier transform ($|F\{G\}|$). The maximal spatial frequency of the Fourier transform was 1/(2 × 0.075μm) = 6.67cycles/μm, where 0.075 μm is the pixel size in the space domain. For better visualization, ω is cropped at 4 c/μm. (*B* and *C*) HBP (*B*) and LBP (*C*) filter and transfer functions, $f_{\text{filter}}(\omega)$ and $\hat{H}(\omega_x, \omega_y)$, correspond to Eqs. 4 and 2, respectively. The theoretical MTF(ω) for confocal microscopy is shown by the red trace (NA = 1.3, λ = 590 nm, n_{medium} = 1.33, d_{pinhole} = 1.2 Airy units or resels (1 resel = 0.61λ/NA); see Eqs. S1–S6 and Figs. S1 and S2 in Data S1). (*D* and *E*) Fluorescence images after filtering ($G'(x, y)$). Intensities can be directly measured by averaging pixel values in regions of interest, as indicated by the red dashed line. Scale bar, 5 μm. Fluorescence intensity is given in photoelectrons (the used gain settings resulted in 1.9 gray value units/photoelectron). Images are printed at $\gamma = 1.6$. See example for filtering in Data S2.

integer numbers (to match the discrete ω values of the discrete Fourier transformation). The HBP and LBP filters were searched between 1 and 4 cycles/μm (c/μm) and between 0 and 2 c/μm, respectively. The common order was searched between 10 and 50. The TR technique using optimized parameters was uniformly applied to an entire set of experiments, which were done using the same optical configuration and fluorophore (Fig. 2, B–D). The Mathematica language implementation of the filtering and optimization is available in Supplementary Material, Data S2.

Model mitochondria for the demonstration of the TR technique

Images modeling fluorescent mitochondria as fluorescent capsule bodies were generated by Mathematica 5.2. Zero-length (l) mitochondria were drawn as spheres of given diameter (d), and elongated mitochondria as l-length, d-diameter cylinders capped with d-diameter half-spheres at both ends. Images of mitochondrion models (512 × 512 pixels) were generated by considering the capsule bodies as solid and fluorescent. The projected fluorescence intensity in the image was calculated using bilinear interpolation for subpixel accuracy: intensity of each pixel of the image was calculated as the mean of intensities of the model in the four corners of the pixel (see details and Eqs. S13–S15 and Fig. S7 A in Data S1). To model shortening of

mitochondria, the following equation system was used to describe the surface and volume of capsule bodies and spheres (Eq. 6):

$$s_{\text{total}} = n(\pi d^2 + l\pi d) \quad v_{\text{total}} = n\left(\frac{\pi d^3}{6} + \frac{l\pi d^2}{4}\right) \quad (6)$$

$$\frac{s_{\text{total}}}{v_{\text{total}}} = \frac{4}{3l + 2d} + \frac{4}{d}, \quad (7)$$

where d is the diameter, n is the number of capsule bodies, and l changes from 7.5 to 0 μm. The solutions of Eq. 6 were used to determine d at the arbitrary $n = 100$ for swelling, or n and d at the constant v_{total} for fission at the indicated (initial for swelling) $s_{\text{total}}/v_{\text{total}}$ ratios. For fission, v_{total} was set to have 100 models initially at each $s_{\text{total}}/v_{\text{total}}$ ratio (for details of modeling, see Eqs. S10–S13 and Fig. S7 in Data S1).

Image and data analysis, statistics

Image processing was carried out using a custom-developed image analysis software written in Pascal language (Delphi 6.0, Borland, Austin, TX) using the fast Fourier transformation of the Intel Image Processing library 2.5 (Intel Corporation, Santa Clara, CA). Filter design and image processing was
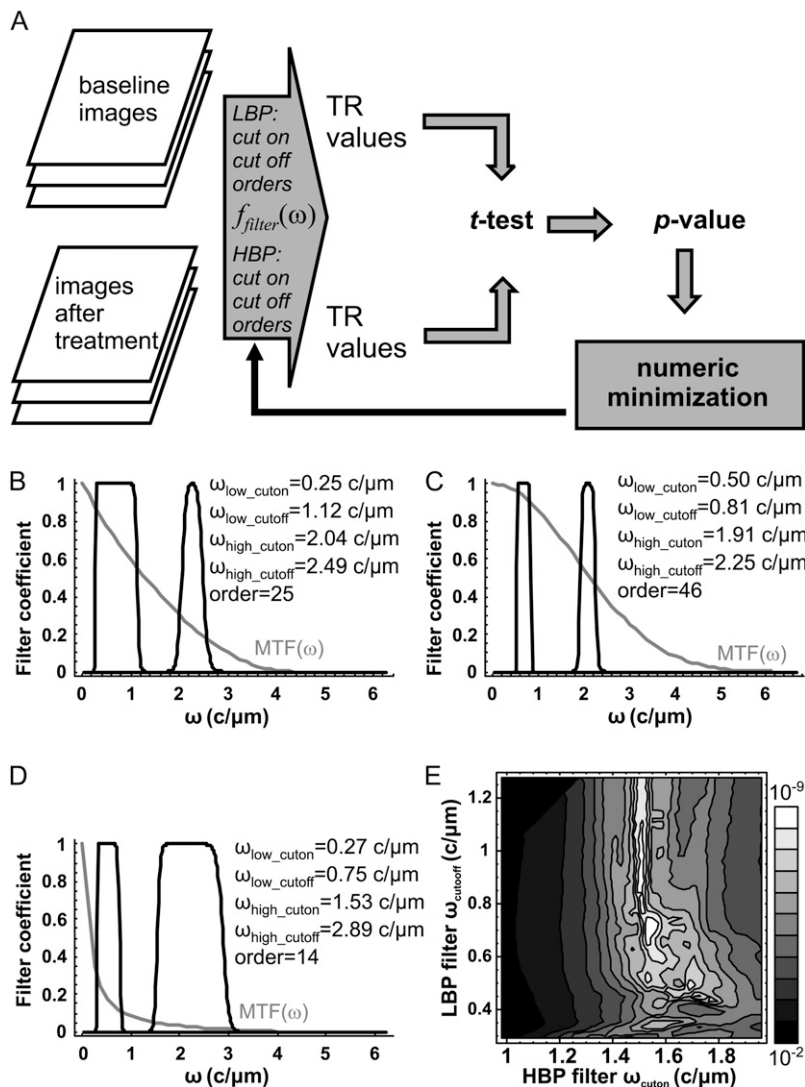

FIGURE 2 Optimization of the filter functions. (A) Scheme of the optimization. Parameters of the two filter functions corresponding to the HBP and LBP filters were determined by numeric optimization using differential evolution to find the global minimum of the p-value. (B–D) Filter functions optimized for alamethicin-evoked mitochondrial swelling in different microscope configurations. Filters are shown without normalization (Eq. 5). Optimized filter functions for wide-field imaging on astrocytes (B) (recorded as single-image plane; λ ≈ 590 nm, 0.1 μm/pixel, NA = 1.3, corresponding to Fig. 5), confocal imaging of neurons (C) (recorded as mean-intensity projected z-stacks; λ ≈ 590 nm, 0.075 μm/pixel, NA = 1.3, corresponding to Fig. 8), and wide-field imaging of mixed cortical cultures (D) (recorded as mean-intensity projected z-stacks; λ ≈ 535 nm, 0.1 μm/pixel, NA = 1.3, corresponding to Fig. 10). (E) Contour plot showing p-values of the optimization in a logarithmic scale as a function of ω_{cutoff} of the LBP filter and ω_{cuton} of the HBP filter. The diagram was generated on the same image sequence that was used for the optimization in D. The other three parameters were taken from D. See example for NMinimize in Data S2.

performed in Mathematica 5.2 by controlling the custom image analysis software through Mathlink. The Pascal implementation of the differential evolution optimization was based on the ''DE/rand/1'' algorithm using population = 100, weight = 0.5, and crossover = 0.5–0.8 to achieve convergence in 50–70 generations (15). All further data and statistical analysis were done in Mathematica 5.2.

RESULTS

Mitochondrial swelling measurement by the TR technique

Mitochondria of cortical astrocytes and neurons in primary cultures were labeled by transient transfection with plasmid vectors encoding mitochondrially targeted DsRed2 (mito-DsRed2; Fig. 1 *A*) or redox sensitive GFP (mito-roGFP1) (12,16). Mitochondrial swelling was analyzed in wide-field and laser scanning confocal micrographs.

We define the TR technique as the calculation of the ratio of fluorescence intensities in the HBP-filtered fluorescence image over the LBP-filtered image. Thin filamentous mitochondria contribute more to the fluorescence intensity measured in the HBP-filtered image (Fig. 1 *D*) than to that in the LBP-filtered one (Fig. 1 *E*). This yields a high TR. In contrast, swollen mitochondria contribute more to the intensity measured in the LBP-filtered image, yielding a lower ratio. The original fluorescence intensity of the raw image cancels due to the ratio calculation; therefore, the TR technique is intensity-independent.

The output of the TR technique is determined by the characteristics of the bandpass filters (Fig. 1, *B* and *C*). The goal of the filter optimization (Fig. 2 *A*) is to maximize the sensitivity of the TR technique for the biological change depicted by a calibration image series (see Methods). Because spatial filtering is strongly related to the modulation transfer function (MTF) of the microscope optics (see Figs. S1–S3 in Data S1), the optimization was performed for each different optical configuration used in this study: 1), for single-plane wide-field microscopy (astrocytes (Fig. 2 *B*)); 2), for *z*-stacking confocal microscopy (neurons (Fig. 2 *C*)); and 3), for *z*-stacking wide-field microscopy (mixed cortical cultures (Fig. 2 *D*)).

The TR technique estimates the diameter of mitochondria at subpixel resolution

The relationship between mitochondrial diameter and the TR was investigated using computer-generated models ranging in diameter around the observed size of mitochondria (Fig. 3, *A* and *B*). Model mitochondrion images consisted of 100 solid fluorescent spheres or elongated-capsule bodies projected into the image plane at random orientation (see also Fig. S7 in Data S1). Model images were generated at the same dimensions and scaling as the acquired fluorescence images. To simulate microscope optics, images were blurred with the MTF of an ideal wide-field or confocal microscope

corresponding to the optical configurations used in this study (Fig. 2, *B* and *C*, and see Figs. S2 and S3 and Eqs. S1–S6 in Data S1). The TR filter functions used with the biological samples below were evaluated using the model images. Fig. 3, *C* and *D*, demonstrates that the TR decreases when the diameter increases. To draw models increasing in diameter by 1/4-pixel increments, bilinear interpolation was used (Fig. S7 *A* in Data S1). The resulting pixel intensities reflect the extent of the overlap between the area covered by the pixel and the model capsule body. The relationship between the diameter and the TR is close to linear ($r^2 > 0.995$) in the range indicated by arrows. It is worthy of note that the TR responds with a slope for the increase of diameters of spheres (Fig. 3 *C*) steeper than that for the increase of elongated structures (Fig. 3 *D*). This feature is exploited below to distinguish mitochondrial swelling from fission.

To assess the theoretical sensitivity of the TR technique, model mitochondria were generated ranging between 3 and 3.5 pixels in diameter, increasing by 1/128-pixel increments (Fig. 3 *E*). These model images had the same dimensions, and models were generated with the same algorithm as above. It is remarkable that the technique resolves 1/128 incremental increases in the diameters of elongated capsule shapes if the shapes are positioned in the same place in each image (*black trace*). If the random orientation of the capsule shapes is different in each image (considering the motion of mitochondria), noise appears (*gray trace*). Still, the technique resolves a 0.15-pixel (~15 nm, considering a typical 0.1 μm/pixel calibration) difference in diameter at a $p < 0.05$ significance level for 100 mitochondria/image and five repeats.

The TR technique was also tested in wide-field-microscope-acquired images of fluorescent beads (TetraSpeck, Invitrogen) of different diameters. Fig. 3 *F* confirms the simulation finding (Fig. 3 *C*, *circles*) that the diffraction-limited resolution of optical microscopy (Rayleigh limit) is not a limit for the TR calculation over sub-resolution-sized objects (see Discussion).

The TR technique and the ''thread-grain'' transition of mitochondria by fission and swelling

The early discovery of dynamic shape changes of mitochondria is reflected in the word ''mitochondrion'', fabricated from the Greek ''mithos'' (thread) and ''chondros'' (grain) in the early 20th century based on light microscope observations (see 17,18). Nevertheless, it is important to realize that the mechanistically and geometrically different processes of mitochondrial fission and swelling both can lead to formation of spherical (grain) mitochondria from ''threads'' (Fig. 4, *A* and *B*). To distinguish these two phenomena, we use this working hypothesis: 1), fission is defined by the increased number of mitochondria at constant total volume, whereas 2), swelling is defined by the constant number of mitochondria at increased volume. Real biological
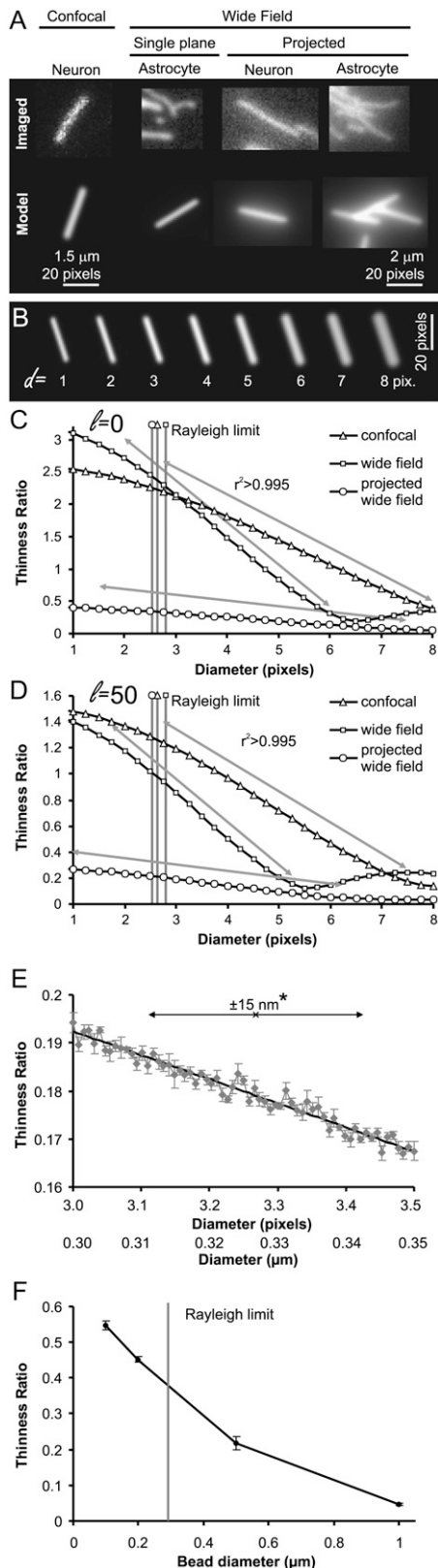
FIGURE 3 The TR technique estimates the diameter of mitochondria. (*A*) Typical imaged mitochondria (*upper row*) and model mitochondrion capsule bodies (*lower row*) are shown at the same printed pixel size. The modeling parameters were dependent on the optical configuration as indicated. Model

phenomena could arise from the combination of the two processes. Further considerations are that 3), the mitochondrial outer membrane determines the optically visible shape of the mitochondrion; and 4), the mitochondrial outer membrane has a constant total surface for the mitochondrial population of a cell. Only the last assumption needs explanation.

The mitochondrial outer membrane cannot be stretched (19). The dynamic, reversible nature of mitochondrial fusion and fission suggests that the mitochondrial outer membrane is unlikely to be consumed or to be inserted during fission. Given the short term of our experiments, mitochondrial biogenesis or turnover is also unlikely to play a role in altering the amount of the mitochondrial outer membrane. In addition, the s_{total}/v_{total} has been shown to be constant throughout the cell cycle (20). It is important to note that the surfaces of individual mitochondria have been shown by three-dimensional (3D) reconstruction of deconvolved confocal volumes to be constant during swelling (21).

To test the effect of ''thread-grain'' transition of mitochondria due to fission or swelling, simulations were performed on model mitochondria of decreasing lengths. We assume that mitochondrial surfaces and volumes can be sufficiently approximated by capsule bodies and spheres. The volume and surface of capsule bodies are given by Eq. 6. For swelling, solutions for v_{total} and d were obtained, and constant n and s_{total} were assumed (Fig. 4, *C* and *E*, and Eq. S11 in Data S1). For fission, Eq. 6 was solved for n and d, and constant v_{total} and s_{total} were assumed; therefore, n and d depend only on l (Fig. 4, *D* and *F*, and Eq. S12 in Data S1). Initial parameters (for large l) were obtained from the electron-microscopic 3D reconstruction literature. Typical diameters of elongated mitochondria reported in dendrites of rat neurons are in the range 200–400 nm (22,23). Mitochondrial surface and volume have been also determined by

mitochondria have diameter $d = 0.34$ μm and are scaled to match the resolution of the acquisition and are blurred by the theoretical MTF of the given optical configuration. (*B*) Model mitochondrion images were generated with increasing diameter and correspond to the confocal microscopic configuration. (*C* and *D*) Effect of mitochondrial diameter on the TR in the three indicated optical configurations using spheres (*C*) or capsules of $l = 50$ pixels (*D*) as models. The model images were blurred with the MTFs given in Fig. 2, *B–D*. Although the slopes are not intended to be used for calibration of real biological data (because the real MTF of the microscope could differ from the theoretical), the reciprocal slopes are given for the estimation of sensitivity in pixels/TR for *C* ($\triangle$, 2.8; $\square$, 1.6; $\bigcirc$, 17.8) and for *D* ($\triangle$, 4.3; $\square$, 3.1; $\bigcirc$, 22.2). (*E*) TR as a function of subpixel changes of the diameter. Model mitochondria were 50 pixels long and were placed in the same positions and orientations in each image (*black trace*) or in a different manner (*gray trace*). The latter simulation was repeated five times and the mean $\pm$ SE is shown. Comparison of all data points by ANOVA with Tukey post hoc test at $p < 0.05$ indicates that data points farther away from each other than an average 0.15 pixels or 15 nm had significantly different TRs. This corresponds to the optical configuration given in Fig. 2 *D*. (*F*) TR (as mean $\pm$ SE of $n = 3$) calculated from fluorescent bead images acquired by mean-intensity projected *z*-stacking wide-field microscopy in conditions similar to the images in Figs. 2 *D* and 10.
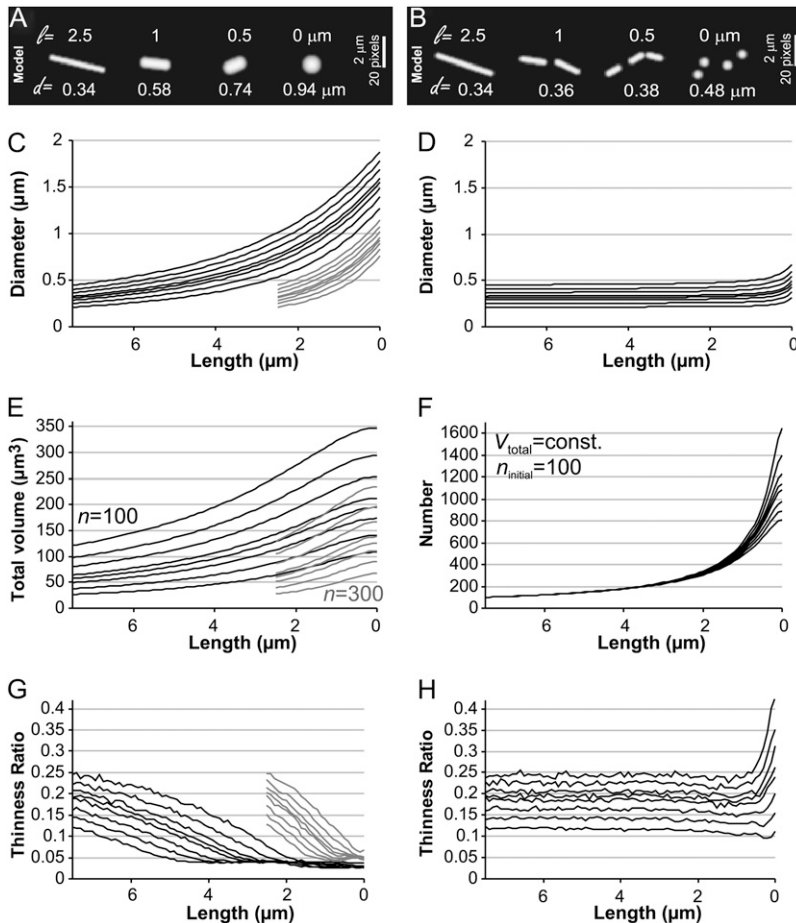
FIGURE 4 ''Thread-grain'' transition of mitochondria: swelling versus fission. (*A* and *B*) Model mitochondria shortening from $l = 2.5$ μm and $d = 0.34$ μm due to swelling (*A*) or fission (*B*). (*C* and *D*) Diameters of model mitochondria calculated as a function of length, based on the considerations of constant n and s_{total} for swelling (*C*) and constant v_{total} and s_{total} for fission (*D*). (*E*) v_{total} as a function of length during swelling. (*F*) Number of mitochondria as a function of length during fission (the starting n was 100). (*G* and *H*) Thinness ratios obtained by filtering blurred model mitochondrion images generated with the parameters given in *C–F* using filter functions shown in Fig. 2 *D*. Traces from top to bottom in *C–E*, and from bottom to top in *F–H* correspond to the starting diameters (in μm) 0.44, 0.40, 0.36, 0.32, 0.30, 0.28, 0.26, and 0.22, or to s_{total}/v_{total} ratios (constant for fission and initial for swelling from $l = 7.5$ μm) of (in μm^{-1}) 9, 10, 11, 12.3, 13, 14, 16, and 19. The simulation of mitochondrial swelling was started from $l = 7.5$ μm (*black traces*) and alternatively from $l = 2.5$ μm (*gray traces*) with the same starting diameters as given above. The results of the fission simulation are fully determined by the constant s_{total} and v_{total}, and therefore do not depend on the initial length.

electron microscopy. By performing calculations from the work of Popov et al. (Table 1 in (22)), the s_{total}/v_{total} yields 12.3 μm^{-1}. Similar ratios ($\sim$10.6 μm^{-1}) have been determined in HeLa cells (20). The $s_{total}/v_{total} \approx 4/d$ if $l \gg d$ (from Eq. 7). The resting diameters of elongated mitochondria observed in our experiments were $d \approx 0.3$–0.4 μm (Fig. 3 *A*), which yields s_{total}/v_{total} of 10–13.3 μm^{-1}. In contrast, at $l = 0$, $s_{total}/v_{total} = 6/d$ (from Eq. 7); therefore, formation of spheres from long mitochondria by fission always leads to a 1.5-times increase of diameter (Fig. 4 *D*).

Model mitochondrion image sequences were generated by placing the calculated (or constant) number of capsule bodies, n, with calculated diameter (d) and independent variable length (l) at random positions and orientations (Fig. 4, *A* and *B*, and Fig. S7 in Data S1). Then, image sequences were blurred with the MTF shown in Fig. 2 *D* to simulate diffraction-limited microscopy.

Shortening of mitochondria during swelling is accompanied by a large increase in diameter (Fig. 4 *C*). Processing the model images with TR filter functions given in Fig. 2 *D* resulted in decreasing and bottoming (saturating) values (Fig. 4 *G*). Therefore, simulation was also started from shorter (initial $l = 2.5\mu$m) models (*gray traces*). In a striking contrast, during mitochondrial fission, the TR (using the same

filter functions as above) is not affected by initial shortening (Fig. 4 *H*). At $l < 0.25$ μm, the TR was altered due to the sphere formation, and the direction of the change was dependent on the s_{total}/v_{total} ratio. It is important to note that this effect is minimal at those resting diameters that are in the range of the physiologically expected value ($d \approx 0.33$–0.4 μm or $s_{total}/v_{total} \approx 10$–12 μm^{-1}; *middle traces*). These findings were typical for all three optical configurations tested (Figs. S8 and S9 in Data S1). We suggest that the greater sensitivity of the TR technique for spherical structures (Fig. 3, *C* and *D*) balances the 1.5-times increase in diameter during fission. Therefore, the TR technique is not sensitive to mitochondrial fission in general; however, in cases of biologically extreme s_{total}/v_{total} ratios, complete fission of mitochondria into the ''grain'' geometry can bias the swelling measurement.

Effects of overlaps between mitochondria are mitigated by the frequency-domain image processing

Some of the above simulations used randomly positioned and oriented model mitochondria (Figs. 3 *E* and 4). The above results indicate that although the random positioning and orientation add noise, the TR is not biased by the position,

orientation, and overlap of mitochondria. Effects of overlaps and closely adjacent mitochondria are greatly mitigated by the frequency domain approach (see Discussion and Fig. S6 in Data S1). Therefore, the TR is also expected to be largely unaffected by mitochondrial motion or aggregation when the mean response of a population of mitochondria is measured.

Measurement of mitochondrial swelling in primary cortical astrocytes

Cortical astrocytes were imaged by time-lapse fluorescence microscopy at high magnification (~0.1 μm pixel size) in a single, fixed plane (Fig. 5 *A*). Flat astrocytes showing moderate mito-DsRed2 expression were chosen for observation. These cells had healthy, elongated, branched mitochondria of even thickness, without periodic dilatations or constrictions. To reproduce a classical, energized mitochondrial swelling experiment, astrocytes were first exposed to 0.2 nM valinomycin, a K$^+$ ionophore, via the superfusate (24,25), followed by application of a high concentration (250 nM) of valinomycin (Fig. 5 *A 2*). As a well established method to calibrate

mitochondrial swelling in isolated mitochondria, the pore-forming peptide alamethicin (40 μg/ml; Fig. 5 *A 3*) was added at the end of each experiment (26–28).

The TR technique was optimized to detect mitochondrial swelling using the above plus two similar image sequences. Two possible approaches were considered for optimization. Sensitivity of the TR technique is maximized by optimization for the minimal change of the baseline morphology during the 0.2-nM valinomycin treatment. In contrast, the dynamic range is optimized by comparing baseline to the largest observed amplitude swelling. Fig. 3, *C* and *D*, and Fig. 4 *G* indicate that that the dynamic range of the TR is limited. Therefore, to evaluate our experiments involving small- and large-amplitude swelling, we chose the optimization for large-amplitude swelling. The geometric mean of *p*-values of alamethicin-evoked TR decrease calculated from three recordings was minimized according to Fig. 2 *A*.

Next, TR was calculated for all experiments in Fig. 5 using the optimized bandpass filter functions (Fig. 2 *B*). Fig. 5 *C* shows the average response of three astrocytes during valinomycin treatment, demonstrating that the TR technique
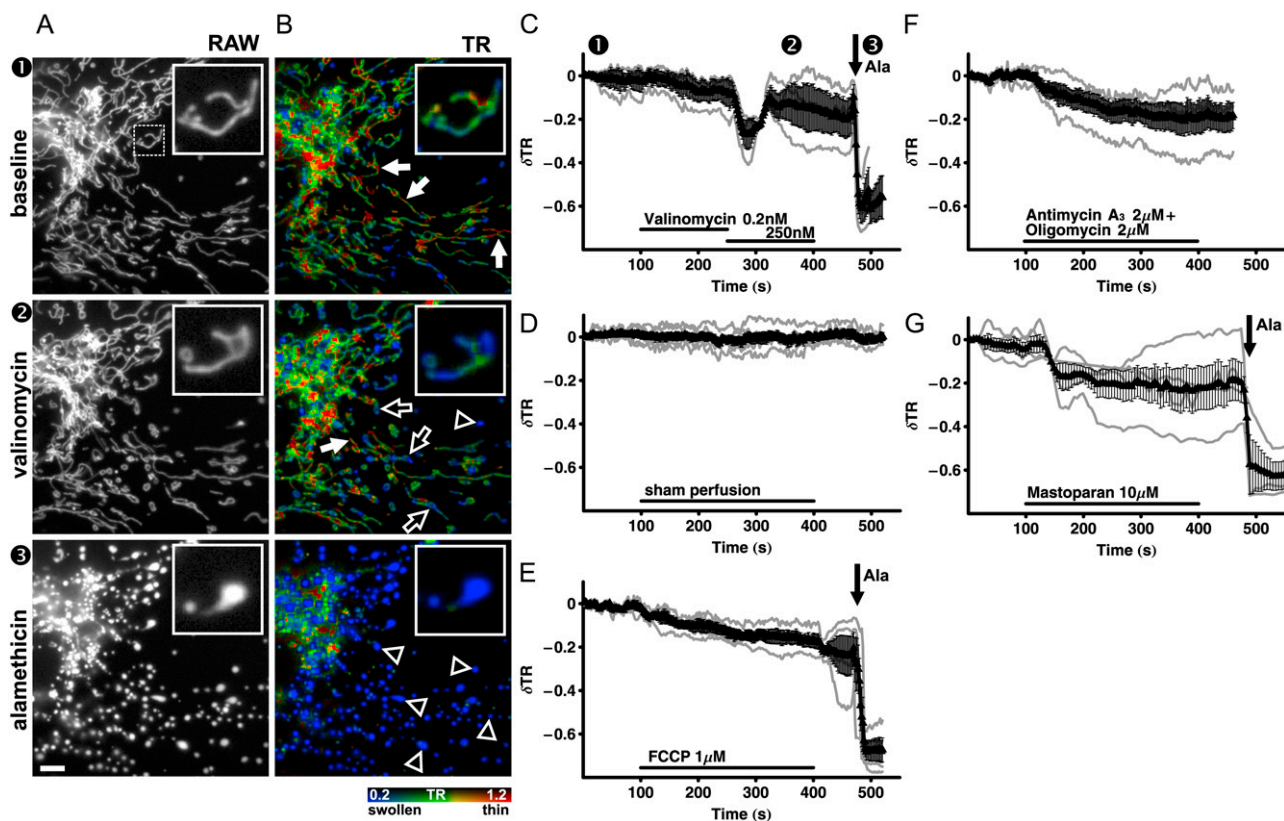

FIGURE 5 In situ mitochondrial swelling in cortical astrocytes. (*A*) Raw fluorescence micrographs of a mito-DsRed2-expressing cortical astrocyte, acquired by single-plane wide-field fluorescence microscopy. (*B*) TR shown as pseudocolor images gated with raw intensity. Solid and open arrows indicate slender and swollen mitochondria, respectively. Open arrowheads indicate swollen, beaded (grain) mitochondria. Scale bar, 5 μm. (*C–G*) Time course of the TR shown as mean ± SE of single cell traces (*gray*) normalized to the baseline ($\delta TR \equiv \Delta TR/TR_0$). (*C*) Effect of valinomycin (0.2 and 250 nM) and alamethicin (*Ala*; 40 μg/ml; $n = 3$). Numbers in black discs refer to the frames shown in *A*. (*D*) Switch of superfusion to identical buffer ($n = 4$). (*E*) Effect of FCCP (1 μM) and alamethicin (40 μg/ml; $n = 3$). (*F*) Effect of antimycin A$_3$ (2 μM) plus oligomycin (2 μM) ($n = 4$). (*G*) Effect of mastoparan (10 μM) and alamethicin (40 μg/ml) ($n = 3$). The filter functions for the TR calculation are given in Fig. 2 *B*.

can distinguish between thin, resting mitochondria and slightly thicker, swollen ones, with the visual appearance only minimally altered. Notably, 250 nM valinomycin caused a transient decrease in the TR signal. The onset and recovery of this transient decrease was likely due to initial swelling followed by formation of ring- or bagel-shaped mitochondria (Fig. 5 *A 2*). Next, we tested the effect of the uncoupler FCCP (1 μM; Fig. 5 *E*), the effect of blocking oxidative phosphorylation by the ATP synthase inhibitor oligomycin (2 μg/ml) combined with the respiratory complex III inhibitor antimycin A$_3$ (2 μM; Fig. 5 *F*), and the effect of the pore-forming wasp toxin peptide mastoparan (26,27) (10 μM; Fig. 5 *G*). All four treatments (Fig. 5, *C* and *E–G*) resulted in a mediocre ($\sim$20%) decrease in the TR compared to the alamethicin-evoked decrease of $\sim$60%. It is of interest that fluorescence images revealed that alamethicin-evoked swelling is manifested in a more extreme manner than that induced by any of the other treatments (Fig. 5 *A 3*; formation of large, spherical organelles, filled with mito-DsRed2). Alamethicin treatment also led to the rupture of the inner mitochondrial membrane and to the release of the tetramer DsRed2 from swollen mitochondria, as revealed by the one-by-one disappearance of largest mitochondria (the calculated molecular mass after cleavage of targeting sequence is 107 kDa, thus substantially larger than could be released through the mitochondrial permeability transition pore, which is permeable for molecules with molecular mass <1.5 kDa).

To provide a comparison to the results of the TR technique, mitochondrial swelling was measured by classical light scatter in isolated brain and liver mitochondria (Fig. 6). Valinomycin responses measured by the decrease in absorbance at 540 nm in suspensions of isolated mitochondria (Fig. 6 *A*) were similar to the in situ measurements in primary cortical astrocytes (Fig. 5 *C*). However, there was a transient decrease in the TR in response to treatment of astrocytes with 250 nM valinomycin, which was not seen in isolated mitochondria. In contrast, mastoparan promoted a greater swelling in isolated mitochondria than in situ (Figs. 6 *B* and 5 *G*, respectively), probably due to the absence of plasma membrane, which could limit the access of mastoparan to mitochondria. Isolated liver mitochondria (Fig. 6 *C*) gave a larger response at low valinomycin concentrations (0.2 nM) than did isolated brain or in situ astrocyte mitochondria.

FIGURE 6 Light-scatter measurement of swelling in isolated mitochondria. (*A* and *B*) Brain mitochondria isolated by percoll gradient were exposed to valinomycin (0.2 and 200 nM) and to alamethicin (*Ala*; 40 μg/ml) (*A*) or to mastoparan (1 and 4 μM) and to alamethicin (*Ala*; 40 μg/ml) (*B*). (*C*) Liver mitochondria exposed to valinomycin (0.2 and 200 nM) and to alamethicin (*Ala*; 40 μg/ml). Gray traces show alamethicin-only treatments; black traces show effects of the indicated treatments. Optical density measured at 540 nm was normalized to a baseline of 1, with a value of 0 after alamethicin treatment. Traces are representative of triplicate measurements.

Inhibition or uncoupling of oxidative phosphorylation does not trigger mitochondrial swelling in primary neuron-enriched cortical cultures

Neuronal mitochondria were more densely packed compared to flattened astrocytes, especially in the soma. Dendritic arbors were substantially stretched in three dimensions compared to the optical thickness (Fig. 7). Therefore, 3D, laser scanning confocal microscopy and *z*-projections of image stacks were us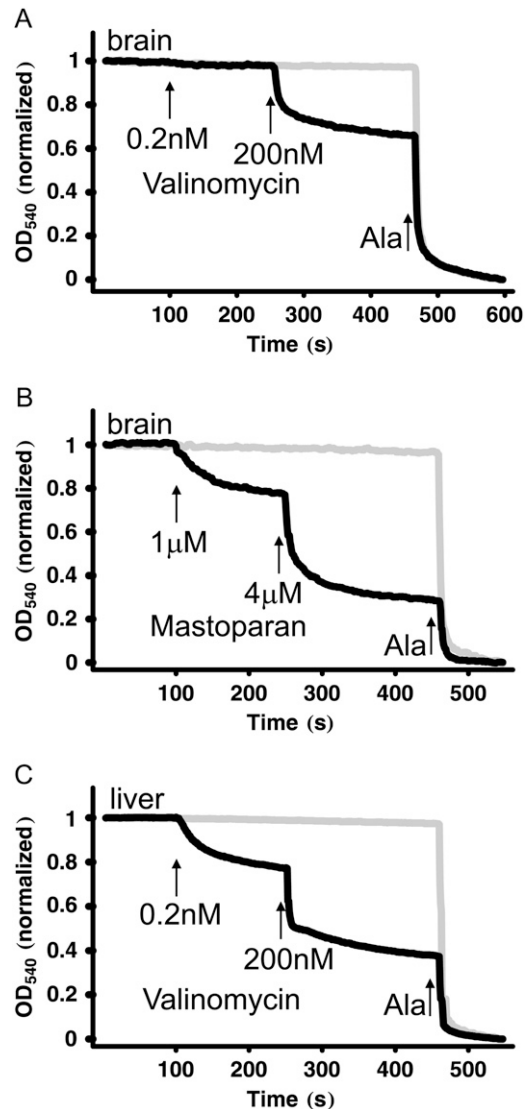ed to obtain in-focus images of a part of the neuronal dendritic arbor. To maintain linearity, which is required for accurate measurements of overlapping objects, mean intensity projection was used (see Figs. S4 and S5 in Data S1). It is noteworthy that the soma of the neurons protruded substantially above the acquired volume, because their complete imaging would require an excessive increase in the number of acquired planes. The fraction of the soma volume imaged can vary by focus drift or swelling of the cell. Consequently, mitochondria were only analyzed in dendrites, not
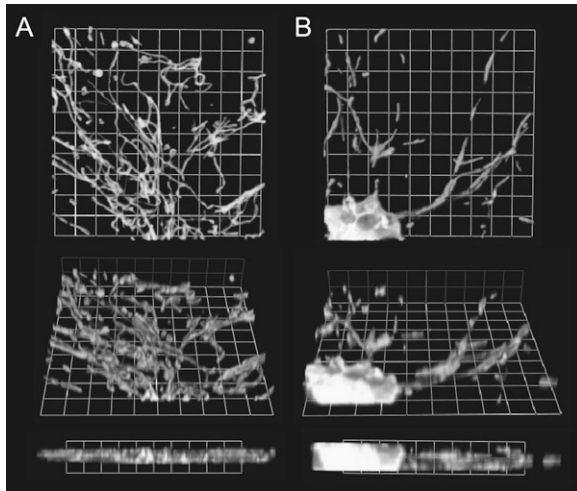
FIGURE 7 Three-dimensional, volume-rendered reconstruction of confocal image stacks. (*A* and *B*) An astrocyte in culture (*A*) and a cortical neuron expressing mito-DsRed2 (*B*). Both image stacks were acquired in identical imaging conditions, with the exception that finer *z*-steps were used for astrocytes. Grid, 3.3 μm. Note that whereas most mitochondria are in a single plane in the astrocyte, mitochondria in neurites are often at different *z*-coordinates, and only a section of the soma was acquired.

in the soma, for Fig. 8. The TR technique was optimized on the effect of alamethicin (40 μg/ml), as detailed above.

Relative responses to valinomycin (200 nM) and alamethicin (40 μg/ml) treatments were smaller in neurons (Fig. 8, *A–C*) than in astrocytes (Fig. 5). It is striking that discharge of mitochondrial membrane potential mediated either by FCCP (Fig. 8 *E*) or by a combination of oligomycin plus antimycin A$_3$ (Fig. 8 *F*) did not decrease the TR. Mastoparan (10 μM) was also ineffective in triggering neuronal mitochondrial swelling (Fig. 8 *G*).

Antimycin A$_3$ plus oligomycin triggers mitochondrial fission in neurons

Oligomycin plus antimycin A$_3$, but not FCCP, treatment of cortical neurons triggered dramatic fission of elongated mitochondria into a multitude of smaller organelles (Fig. 8 *H*). It is important that this did not lead to a change in the TR (see above; Fig. 8 *F*). This result could be considered supporting evidence of our above prediction that fission of mitochondria has little effect on the TR (Fig. 4 *F*).

3D wide-field microscopy is optimal for the TR technique

The above experiments demonstrated that the TR technique is applicable for both wide-field and confocal microscopy. To find the ideal settings for the microscopy, the signal/noise ratio (SNR) was estimated by modeling of error propagation through the TR calculation (Eqs. S5–S9 in Data S1). To do this, a simplified model of TR technique was used: the TR was cal-

culated as the ratio of integrals of the MTF between ω_{cuton} and ω_{cutoff} for the HBP over the LBP filters. To demonstrate the effects of different optical parameters on the filtering technique, all calculations were done using the filter functions described in Fig. 2 *D*, regardless of simulated optical configuration. The obtained values reflect the TR of the point spread function (PSF) of the microscope, which is the thinnest possible detail, and is thus the theoretical maximum of the TR. The SNR (or TR/standard deviation) was calculated by considering a mean signal of 1000 pixels at ~1000 photoelectrons/pixel mean intensity. Fig. 9 *A* indicates that the SNR monotonously increases with the pinhole diameter. Fig. 9, *B* and *C*, shows the dependence of the SNR on NA at constant mean fluorescence intensity. It is worthy of note that these diagrams dissect only the spectral effects of NA on the TR. The mean fluorescence intensity increases with NA^4 (29); therefore, higher NA always yields higher SNR. Fig. 9, *B* and *C*, also indicates that a similar SNR can be achieved at the same detector photon count with confocal and wide-field microscopy. The SNR is only slightly dependent on the emission wavelength of the fluorophore (Fig. 9 *D*). The SNR is proportional to the square root of the fluorescence intensity (Fig. 9 *E* and Eq. S9 in Data S1); therefore, the higher photon collection efficiency of the wide-field microscopes with CCD cameras makes them more suitable for the TR technique. In Fig. 9 *E*, an effect of mitochondrial swelling (and therefore a decrease in the TR) on the SNR was demonstrated by decreasing the value of the above calculated high-frequency integral (Eq. S8 in Data S1) to obtain the indicated arbitrarily chosen TR value.

The sensitivity of the TR technique was assessed by finding the absolute ΔTR for each SNR that results in a $p = 0.05$ with Student's *t*-test comparison of five *TR* and five *TR* + ΔTR values. Fig. 9 *F* indicates that the sensitivity benefits only slightly from SNRs >~500, which corresponds to 1000–2000 photoelectrons/pixel (Fig. 9 *E*). Fig. 9, *E* and *F*, suggests that photon shot noise at typical acquisition conditions is not a limitation of the technique, as compared to the error that originated from the mitochondrial motion (Fig. 3 *E*).

Comparison of mitochondrial swelling in neurons and astrocytes in mixed cortical cultures

The differences in neuronal and astrocytic mitochondrial swelling were verified by parallel measurements in both cell types in mixed cortical cultures in the same experiments (and optical configuration). Based on the above theoretical considerations, wide-field *z*-stacking with mean intensity projection was used to capture images. Eight-well-coverglass bottomed culture dishes were mounted on the motorized stage of the microscope, and the seven conditions shown below were imaged at baseline, at 5 min, and at 90 min after treatment in a time-shifted manner in the same multiwell dishes. Five cells, a combination of neurons and astrocytes expressing mito-roGFP1, were imaged in each well. To
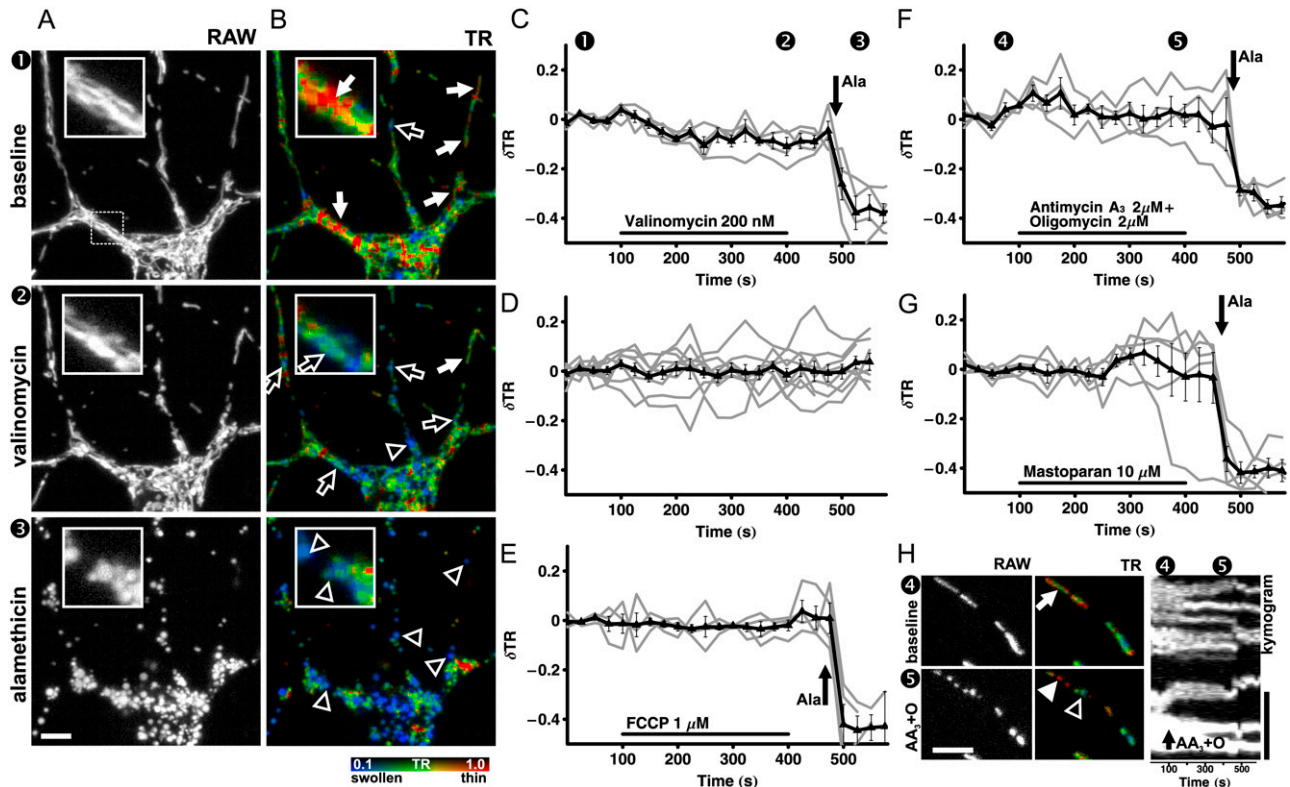
FIGURE 8   In situ mitochondrial swelling in cortical neurons. (A) Fluorescence micrographs of mito-DsRed2-expressing cortical neurons acquired by laser scanning confocal microscopy, shown as maximum intensity z-projections. (B and H) TR shown as pseudocolor images gated with raw intensity. Solid and open arrows indicate slender and swollen mitochondria, respectively. Open arrowheads indicate swollen, beaded mitochondria. Scale bar, 5 μm; zoom 2.5$\times$. (C–G) The time course of TR is shown as mean $\pm$ SE of single-cell traces (gray), calculated with the filters shown in Fig. 2 C from mean-intensity projected z-stacks and normalized to the baseline (δ). (C) Effect of valinomycin (0.2 and 250 nM) and alamethicin (Ala; 40 μg/ml) (n = 4). Numbers in black discs refer to the frames shown in A and B. (D) Baseline (n = 9). (E) Effect of FCCP (1 μM) and alamethicin (40 μg/ml) (n = 4). (F and H) Effect of antimycin A_3 (2 μM) plus oligomycin (2 μM) and alamethicin (40 μg/ml) (n = 4). Numbers in black discs refer to the frames shown in H. (G) Effect of mastoparan (10 μM) and alamethicin (40 μg/ml) (n = 5). (H) Antimycin A_3 plus oligomycin triggers mitochondrial fission (depicts F). (Left) Raw and TR pseudocolor images are shown in a manner similar to that in A and B. (Right) The kymogram shows the time course of mito-DsRed2 raw fluorescence along a broken line following the dendrite containing the mitochondria. The filter functions for the TR calculations are given in Fig. 2 C.

prevent excitotoxic mechanisms evoked and amplified by bioenergetic inhibition (30,31), the experimental medium was supplemented with the NMDA receptor inhibitor MK-801 (10 μM), the AMPA receptor inhibitor NBQX (10 μM), and the inhibitors of voltage-dependent Ca^{2+} and Na^+ channels, nifedipine (1 μM) and tetrodotoxin (1 μM), respectively. Neurons and astrocytes were distinguished by their different ''mitochondrial'' morphology (Fig. 7), but cultures were also fixed at the end of the experiments and processed for immunostaining for the neuronal marker microtubule-associated protein 2 (MAP2) and the astrocyte marker glial fibrillary acidic protein (GFAP) (Fig. 10, E and H). The TR filter functions were optimized on the effect of alamethicin in a pool of three astrocytes. These filters were applied uniformly for the whole dataset in both cell types.

Fig. 10, A and B, shows changes of TR relative to the baseline in astrocytes and dendrites, respectively, of neurons. In astrocytes, all of the applied treatments resulted in significant changes of TR compared to the baseline after 5 min (# symbols), and most were significantly different from the

vehicle (ethanol) treatment (stars). Conversely, in neurons, only 200 nM valinomycin had a significant effect. Although both cell types exhibited mitochondrial swelling after 90 min, the swelling in neurons (including the alamethicin-evoked) was only half or less than half as extensive as in astrocytes. This verifies the absence of mitochondrial swelling in neurons for short-term FCCP or oligomycin plus antimycin A_3 treatments. Identical conclusions can be drawn from data obtained with TR filter functions optimized on neurons (Fig. S10 in Data S1). Analysis of mitochondria in the soma of neurons also supports this conclusion (though less reliably, as noted above), as these mitochondria behaved similarly to the mitochondria observed in the dendrites (Fig. S10 C in Data S1). The difference between astrocytes and neurons was also qualitative: whereas astrocytic mitochondria beaded up and formed ''bagels'' upon bioenergetic inhibition, neuronal mitochondria kept their slender, elongated shape (Fig. 10, D and G). These findings indicate that mitochondrial swelling is generally limited in cortical neurons compared to astrocytes. It is worthy of note that we did not observe fission of neuronal
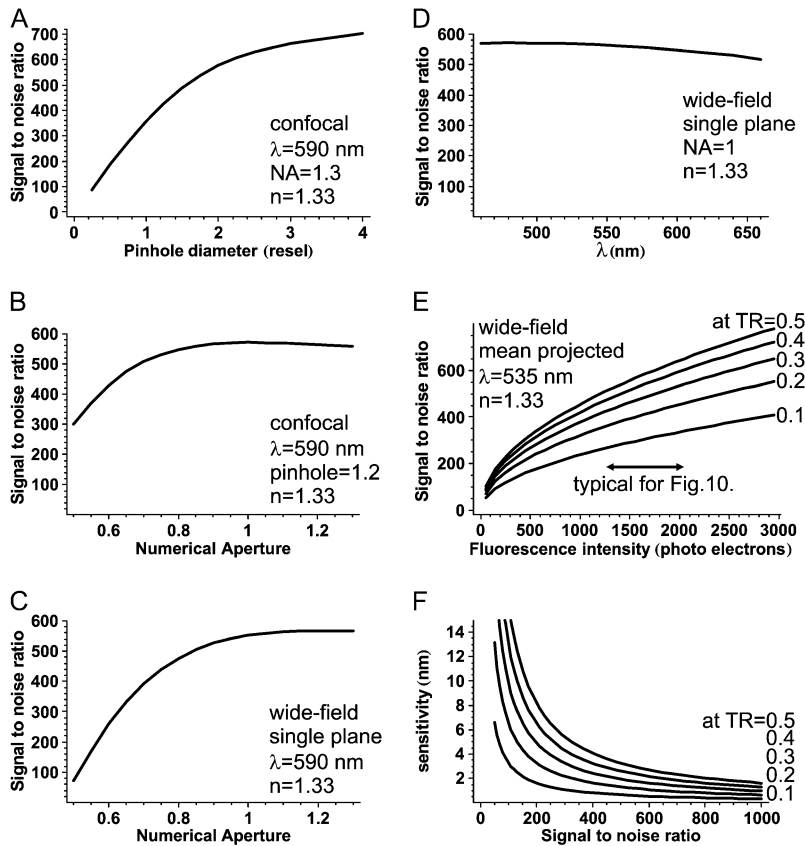
FIGURE 9 Signal/noise ratio of the TR in different optical configurations. (*A*) SNR as a function of confocal pinhole size (1 resel = 0.61λ/NA). (*B* and *C*) SNR as a function of NA for confocal and wide-field microscopy, respectively. (*D*) SNR as a function of emission wavelength (λ). (*E*) SNR as a function of the mean fluorescence intensity of the PSF. The intensity units are given in photoelectrons; therefore, the variance of photon shot noise equals the intensity. Arrows show the typical detection range. For this, the sum of photoelectrons from seven image planes and 0.4 gray value units/photoelectron were used. (*F*) Sensitivity of the TR technique as a function of SNR. Sensitivity was defined as the absolute change of the TR, which results in $p = 0.05$ in a two-tailed Student's *t*-test comparison of two sets of five samples (calibrated to nanometers based on Fig. 3 *D* (*circles*) at 2.2 μm/TR. (*E* and *F*) The indicated arbitrary TR values were generated by decreasing the high-frequency integral component in Eq. S8 in Data S1, and this was followed by calculation of error propagation.

mitochondria for the oligomycin plus antimycin A_3 treatment in the presence of the antiexcitotoxic blockade.

DISCUSSION

The thinness ratio, or optimized spatial filtering technique, is a novel fluorescence-microscopic image-processing technique. This technique provides quantitative, single-cell, in situ measurement of mitochondrial swelling. The TR decreases proportionally with the increase of the diameter of mitochondria during mitochondrial swelling and is specific to mitochondrial swelling as compared to mitochondrial fission. The technique is sensitive to diameter increases at 10 nm scale. Using the TR technique, we provide further evidence on the difference in physiology between astrocytic and neuronal mitochondria, namely, that short-term bioenergetic inhibition causes marked mitochondrial swelling in astrocytes, but not in cortical neurons. It is important to note that the TR technique does not require a specialized microscope or hardware design, but is based upon computational analysis of wide-field or confocal fluorescence micrographs of fluorescent proteins expressed in mitochondria of specific cell types.

Optical measurement of mitochondrial swelling

The classical detection of mitochondrial swelling by light scatter reflects ultrastructural changes in matrix volume and

density (32), cristae configuration (33,34), contact site formation between inner and outer membranes (35), and changes in particle shape and size (10). In addition, light scatter is extremely sensitive to non-swelling-related optical changes, such as accumulation of calcium-phosphate precipitate in mitochondria (36).

One alternative in situ approach to measure mitochondrial swelling is the tissue or single-cell angular light scatter (10). It is of interest that this technique is also based on bandpass spatial filtering and ratioing, although with a very different approach, using a specialized optical design in a transmitted-light microscope. Another, more widely used fluorescence microscopic image processing technique relies on binarization, segmentation, and shape measurements. This includes calculation of roundness (or form factor) from the area and circumference of the segmented shapes (8). Both alternative techniques are sensitive to mitochondrial fission. It is important to note that we have shown that the TR technique is not sensitive to mitochondrial fission. The isosurface measurement is a 3D extension of the segmentation and shape measurement technique, and provides precise volume and surface information of individual mitochondria acquired by deconvolution confocal microscopy (21). In contrast to the TR technique, isosurface measurement requires mitochondria to be well separated from each other, and is based on excessive image acquisition (number of planes and resolution) and computation.
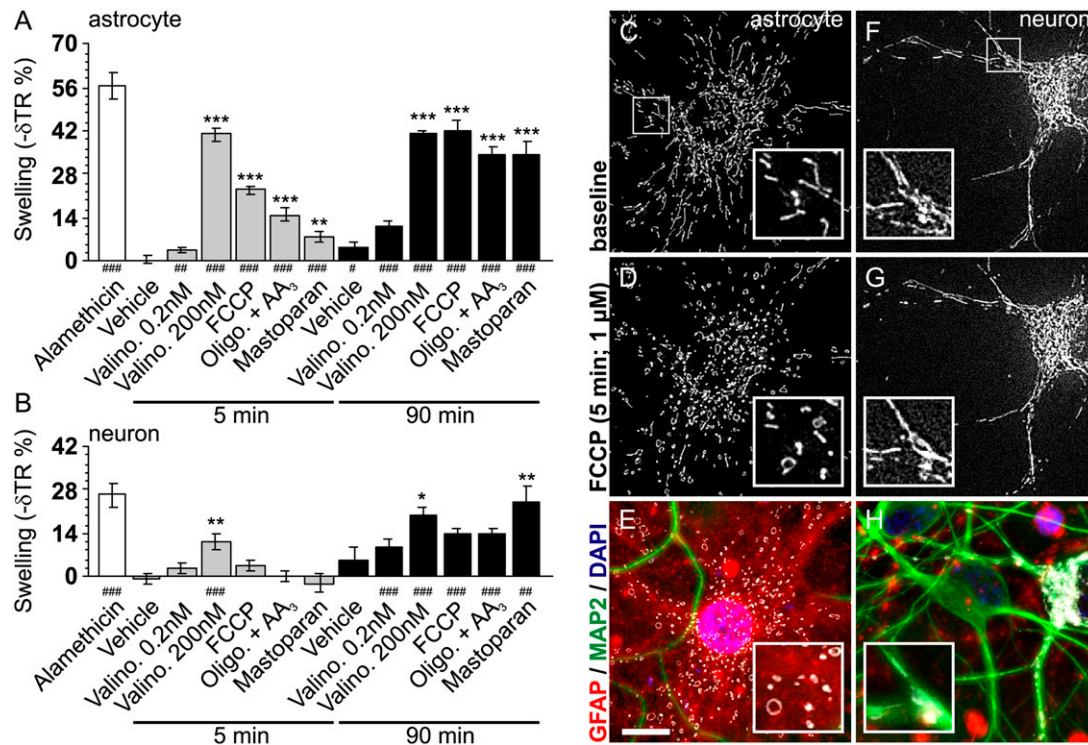
FIGURE 10   Comparison of astrocytes and neurons in mixed cortical cultures. (*A* and *B*) Mitochondrial swelling is indicated as a percentage of negative change of the TR. The TR was measured at baseline, and after 5- and 90-min treatment with vehicle (1:1000 ethanol), valinomycin (0.2 and 200 nM), FCCP (1 μM), and oligomycin (2 μg/ml) plus antimycin A$_3$ (1 μM) or mastoparan (10 μM). Bars indicate mean $\pm$ SE of baseline-normalized negative TR for the 5-min treatment (*gray bars*) or the 90-min treatment (*black bars*). The maximal-effect alamethicin (20 μg/ml) was captured after addition without delay, because of progressive lysis of mitochondria. #, $p < 0.05$; ##, $p < 0.01$; and ###, $p < 0.001$ compared to 0 by two-sided Student's t-test. *$p < 0.05$, **$p < 0.01$, and ***$p < 0.001$ compared to the vehicle treatment by ANOVA for the given time point with Dunnett's post hoc test. A representative astrocyte (*C–E*) and a neuron (*F–H*) from the same experiment are shown at baseline (*C* and *F*), after 5 min FCCP (1 μM) treatment (*D* and *G*), and after fixation at $\sim$2 h and staining for the astrocyte marker GFAP (*red*), neuronal marker MAP2 (*green*), and nuclear marker DAPI (*blue*) (*E* and *H*). Scale bar, 10 μm. Data are from four independent cell culture preparations and $n > 10$ cells for each condition. The filter functions for the TR calculations are given in Fig. 2 *D*.

Fluorescent micrographs showing matrix-targeted fluorescence proteins carry information regarding the shape of the matrix space. The configuration of the matrix, i.e., how much space cristae take from the matrix, cannot be resolved by light microscopy, but is reflected as a dilution of local fluorescence intensity (37). The TR technique is insensitive to changes in intensity and therefore to changes in matrix configuration, because of the ratio calculation. Thus, the TR technique selectively measures the bulk shape of the matrix space. The insensitivity to intensity changes is also a significant advantage of the TR technique over binarization- and segmentation-based techniques if the sample has both dim and bright regions, or if the intensity changes in time.

Subresolution and subpixel measurement of mitochondrial diameters by the TR technique

The average diameter of mitochondria in cortical neuronal cultures observed in 3D electron microscopic reconstruction (22,23) ($\sim$200–400 nm) is approximately equal to the resolution limit of light microscopy given by the Rayleigh criterion (29) ($0.61\lambda/\text{NA} = 0.61 \times 590\,\text{nm}/1.3 = 278\,\text{nm}$) for DsRed2.

However, the Rayleigh limit is a subjective criterion for the distinction of nearby objects (38). Mathematically, the image formation by the microscope is considered as convolution of the object with the PSF of the optics. Using this model, the TR is not limited by the optical resolution (Fig. 3, *C* and *D*), and this was also confirmed experimentally by using fluorescent beads (Fig. 3 *F*). Considering the image formation convolution in frequency domain, the ω components of the subresolution object are multiplied with the MTF of the optics. The information used for TR calculation is provided by those ω components of the subresolution objects that are transmitted by the bandpass filters. It is important to note that these frequencies are also transmitted by the MTF, because the ω_{cutoff} of the HBP is below the cutoff of the MTF (which is the largest spatial frequency transmitted by the optics). The ω components corresponding to the ω range of the LBP and HBP filters are multiplied by the larger-than-zero MTF(ω) values; therefore, the TR is scaled by factor times depending on the actual MTF of the optics, but no information is lost. Thus, subresolution size information is detected by the TR technique.

The TR technique also overcomes the limitations of the detector resolution. The subpixel resolution of size changes

can be explained by the following features of Fourier domain spatial filtering. The bandpass filters are rotational symmetric; therefore after filtering, the intensity information reflects a ''360° panoramic view'' on the size (considering objects parallel with the image plane). This is why elongated objects yield smaller TRs than circular ones of the same diameter. Fourier domain also resolves fractional pixel wavelengths above $\lambda = 2$ pixels. Thus, pixel-to-pixel gray value gradients in space can be conveniently exploited in the Fourier domain. For example, it is difficult to define a difference between 2.2-pixel and 2.5-pixel thickness of mitochondria in the spatial domain, whereas frequency components with a 4.4- or 5-pixel period length (corresponding to double the diameter) are well separated at $\omega = 116$ and 102 pixels, respectively, in the Fourier domain of a 512×512 image. It is suggested that both the averaging resulting from the rotational symmetry and the frequency component resolution play a role in the subpixel resolution.

The ideal imaging device (CCD camera or confocal scanner) should be able to capture spatial frequencies double that of the ω_{cutoff} of the HBP filter to fulfill the Nyquist sampling theorem. For example, because a typical ω_{cutoff} was 2.5 c/μm in this study, the imaging resolution should be $1/2\omega_{\text{max}} = 1/(2 \times 2 \times 2.5 \text{ c}/\mu\text{m}) = 0.1 \ \mu\text{m/pixel}$, or, if compromise is required, at least double the ω_{cuton} of the HBP, which yields 0.14 μm/pixel for 1.8 c/μm.

The subpixel resolution is a major advantage of the TR technique over binarization- and image-segmentation-based techniques. Another advantage of the frequency-domain image processing is the reduced bias due to overlaps of mitochondria. Overlapping objects are perceived as a superposition of sine waves, and therefore, the TR reflects (intensity-weighted) average diameters of individual mitochondria within agglomerates, as long as there is a minimal contrast between them (Fig. S6 in Data S1).

The sensitivity is limited by error of biological origin

The sensitivity of the technique is determined by the biological variability due to motion and overlaps of mitochondria (Fig. 3 D) in addition to the detector photon shot noise (Fig. 9 E). The sensitivity is not improved by decreasing the shot-noise-originated error to levels below the biologically originated error. Therefore, using stronger illumination intensities, which yield more than 500–1000 photoelectrons/pixel (Fig. 9, D and E) are unnecessary. A photon count of 1000 translates to 400 gray value units above the offset in our CoolSnap HQ CCD camera used at high gain (~0.4 gray value units/photoelectron) and $400/7 = 57$ units in mean-projected seven planes.

The treatment conditions applied in this study had homogeneous and synchronous effects in the mitochondrial population of the view field. In contrast, heterogeneous mitochondrial swelling was observed in excitotoxic glutamate-

treated neurons by electron microscopy (39); therefore, these conditions will be an interesting matter of TR image or single-mitochondrion TR calculation.

The choice of the microscope

Modeling indicates (Fig. 9 and Eqs. S7–S9 in Data S1) that in confocal microscopic configuration, the SNR of the TR monotonously increases as the pinhole opens, because the higher detected fluorescence intensity dominates the decreased transmission of higher spatial frequencies. We conclude that the more efficient photon-collecting wide-field microscopy is the technique of choice for TR measurement. For projection of z-stacks, use of mean-intensity (or accumulation) projection is recommended to maintain linearity, which is required for the accurate measurement of overlapping objects in different planes. The axial resolution of wide-field microscopy in our case was $2n\lambda/\text{NA}^2 = 2 \times 1.33 \times 0.535\mu\text{m}/1.3^2 = 0.84$ μm (29). This was used as the step size for z-stacking. The additional out-of-focus blur in mean projected wide-field z-stacks is affecting only the very-low-frequency part of the MTF, mostly below the typical ω_{cuton} of the LBP (Fig. S5 in Data S1 and Fig. 2 D). Furthermore, the ω_{cutoff} of the HBP is below the cutoff of the MTF (at high NA), and therefore, high NA is not critical for the TR calculation itself. A practical implication is that the TR technique can be used with water immersion lenses. The microscopy parameters suggested for TR determination are summarized in Table 1.

The choice of the fluorophore

Although high quantum yield of the fluorophore is evidently beneficial due to higher fluorescence intensity, the λ of emission has little effect on the TR (Fig. 9). Because the TR calculation is insensitive to intensity changes, fluorescence sensors like the redox-sensitive mito-roGFP1 can be used for mitochondrial swelling measurement. It is important to note the large molecular weight of the fluorescent labeling of mitochondria, which makes targeted fluorescent proteins essential for the correct use of the TR technique. Mitochondrial markers like Mitotrackers can redistribute between

TABLE 1 Optimal parameters of microscopy for mitochondrial swelling measurement with the TR technique

	Important parameters	Additional parameters
Fluorophore	Large molecular weight, organelle-specific, bright	λ is less important, can be a probe
Focus	z-stacking and mean intensity projection	Step size = axial resolution ~0.8 μm
Optics	NA > 0.8, but higher is better; if confocal, pinhole > 1.5 resel	Wide-field (or confocal)
Detector	0.1–0.14 μm/pixel resolution ~1000 photo e^-/pixel (summed for the z-stack)	Use region averaging

mitochondria and the cytosol when mitochondria depolarize or when the permeability transition pore opens. Such redistribution leads to the loss of high spatial frequency components of the image, which results in a decrease of the TR, mimicking mitochondrial swelling. Conversely, we have previously used high-pass filtering at $\omega_{\mathrm{cuton}} = 0.5$ c/μm to reject fluorescence of dyes residing in the cytosol, but transmitting fluorescence of mitochondria with the aim of selective detection of mitochondrially originated fluorescence (11,40). In that case, it was crucial to have a shape-independent detection of mitochondrial intensity, and this was provided by the low ω_{cuton}, which was similar to the typical ω_{cuton} of the LBP filters used in this study.

Neuronal versus astrocytic mitochondria

Mitochondrial swelling in astrocytes and neurons was assayed in different optical systems initially (Figs. 5 and 8), as the TR technique was developed. Because both the SNR (Fig. 9) and the response of the TR to diameter increase (Fig. 3) depend on the optical configuration, the two cell types were finally compared using the same microscopic technique (Fig. 10), which was optimized based on the accumulated data. Astrocytic mitochondria swell, as indicated by the decreased TR, and exhibit characteristic morphological changes during short-term bioenergetic inhibition. In neurons, both the change of TR and the morphological alterations were absent in these conditions. However, neuronal mitochondria also swell after long-term (90-min) treatment. When astrocytes were exposed to alamethicin, tubular mitochondria shortened in length and swelled in width into large spherical structures. This is in contrast to the neurons, where mitochondrial fission and beads-on-a-string formation was typical, followed by a smaller extent of swelling. The maximal change of TR in neurons was about half of the maximal changes found in astrocytes (using the same filter functions). This translates directly to diameters; thus, neuronal mitochondria increase their diameters during maximal swelling half as much as astrocytes.

FCCP and oligomycin-plus-antimycin-A$_3$ treatments of astrocytes evoked characteristic ''bagel'' or ring-shaped mitochondria. Valinomycin (200 nM) evoked transient ''bagel'' formation, which was followed by the appearance of solid swollen mitochondria. The ''bagel'' formation was reversible and seemed to be due to the dilatation of uncharacterized intramitochondrial, nonmatrix structures devoid of the fluorescent marker, and not to tip-to-tip fusion of mitochondria. Because the matrix space seems to be less swollen after ''bagel'' formation, we hypothesize that this process is part of a matrix volume regulatory mechanism in deenergized mitochondria, requiring further exploration. Similar morphological alterations were reported for acetylsalicylate-treated hepatocytes (41) and uncoupler-treated CV1 cells (42). It its important to note that in neurons, we have only rarely observed such ''bagel'' or ring-shaped mitochondria, and these were smaller in size than the ones in the astrocytes.

Thus, the cell-mitochondrion systems behave distinctly in astrocytes and neurons during inhibition of oxidative phosphorylation. Whether it is an intrinsic difference of mitochondria or is because of differences in the intracellular milieu is a matter for further investigation. It is suggested that cell-type-specific differences could arise from differences in the intracellular K$^+$ homeostasis (9), because of different properties of mitochondrial permeability transition pore opening (5) or because of different sensitivity of triggering the mitochondrial fission machinery. The mitochondrial fission factor dynamin-related protein 1 (Drp1) is expressed in highest amounts in the brain (43). A greater expression of Drp1 in neurons, as compared to astrocytes, could account for the observed tendency of neuronal mitochondria toward fission and bead-on-a-string formation, rather than toward swelling and ring formation, as observed in astrocytes. Considering spatially constrained compartments like axons or thin dendrites in neurons, mitochondrial swelling could have deleterious effects on organelle transport (21,44), as axonal clogging has been implicated in neurodegenerative diseases (45). Therefore, it is possible that neurons have developed distinct mitochondrial volume or fission/fusion regulation compared to other cell types to maintain small-sized mitochondria.

SUPPLEMENTARY MATERIAL

To view all of the supplemental files associated with this article, visit www.biophysj.org.

REFERENCES

1. Solenski, N. J., C. G. diPierro, P. A. Trimmer, A. L. Kwan, G. A. Helm, and G. A. Helms. 2002. Ultrastructural changes of neuronal mitochondria after transient and permanent cerebral ischemia. *Stroke*. 33:816–824.

2. Halestrap, A. P. 1989. The regulation of the matrix volume of mammalian mitochondria in vivo and in vitro and its role in the control of mitochondrial metabolism. *Biochim. Biophys. Acta*. 973:355–382.

3. Zoratti, M., and I. Szabo. 1995. The mitochondrial permeability transition. *Biochim. Biophys. Acta*. 1241:139–176.

4. Kristian, T., I. B. Hopkins, M. C. McKenna, and G. Fiskum. 2006. Isolation of mitochondria with high respiratory control from primary cultures of neurons and astrocytes using nitrogen cavitation. *J. Neurosci. Methods*. 152:136–143.

5. Bambrick, L. L., K. Chandrasekaran, Z. Mehrabian, C. Wright, B. K. Krueger, and G. Fiskum. 2006. Cyclosporin A increases mitochondrial calcium uptake capacity in cortical astrocytes but not cerebellar granule neurons. *J. Bioenerg. Biomembr.* 38:43–47.

6. Shalbuyeva, N., T. Brustovetsky, A. Bolshakov, and N. Brustovetsky. 2006. Calcium-dependent spontaneously reversible remodeling of brain mitochondria. *J. Biol. Chem.* 281:37547–37558.

7. Dubinsky, J. M., and Y. Levi. 1998. Calcium-induced activation of the mitochondrial permeability transition in hippocampal neurons. *J. Neurosci. Res.* 53:728–741.

8. Rintoul, G. L., A. J. Filiano, J. B. Brocard, G. J. Kress, and I. J. Reynolds. 2003. Glutamate decreases mitochondrial size and movement in primary forebrain neurons. *J. Neurosci.* 23:7881–7888.

9. Kaasik, A., D. Safiulina, A. Zharkovsky, and V. Veksler. 2007. Regulation of mitochondrial matrix volume. *Am. J. Physiol. Cell Physiol.* 292:C157–C163.

10. Boustany, N. N., R. Drezek, and N. V. Thakor. 2002. Calcium-induced alterations in mitochondrial morphology quantified in situ with optical scatter imaging. *Biophys. J.* 83:1691–1700.

11. Gerencser, A. A., and V. Adam-Vizi. 2001. Selective, high-resolution fluorescence imaging of mitochondrial Ca^{2+} concentration. *Cell Calcium*. 30:311–321.

12. Dooley, C. M., T. M. Dore, G. T. Hanson, W. C. Jackson, S. J. Remington, and R. Y. Tsien. 2004. Imaging dynamic redox changes in mammalian cells with green fluorescent protein indicators. *J. Biol. Chem.* 279:22284–22293.

13. Chinopoulos, C., A. A. Starkov, and G. Fiskum. 2003. Cyclosporin A-insensitive permeability transition in brain mitochondria.: inhibition by 2-aminoethoxydiphenyl borate. *J. Biol. Chem.* 278:27382–27389.

14. Otsu, N. 1979. A threshold selection method from gray-level histograms. *IEEE Trans. Syst. Man Cybern.* 9:62–66.

15. Price, K., R. Storn, and J. Lampinen. 2005. Differential Evolution. A Practical Approach to Global Optimization. Springer, New York.

16. Rizzuto, R., M. Brini, P. Pizzo, M. Murgia, and T. Pozzan. 1995. Chimeric green fluorescent protein as a tool for visualizing subcellular organelles in living cells. *Curr. Biol.* 5:635–642.

17. Bereiter-Hahn, J. 1990. Behavior of mitochondria in the living cell. *Int. Rev. Cytol.* 122:1–63.

18. Skulachev, V. P., L. E. Bakeeva, B. V. Chernyak, L. V. Domnina, A. A. Minin, O. Y. Pletjushkina, V. B. Saprunova, I. V. Skulachev, V. G. Tsyplenkova, J. M. Vasiliev, L. S. Yaguzhinsky, and D. B. Zorov. 2004. Thread-grain transition of mitochondrial reticulum as a step of mitoptosis and apoptosis. *Mol. Cell. Biochem.* 256–257:341–358.

19. Mannella, C. A. 2006. The relevance of mitochondrial membrane topology to mitochondrial function. *Biochim. Biophys. Acta.* 1762:140–147.

20. Posakony, J. W., J. M. England, and G. Attardi. 1977. Mitochondrial growth and division during the cell cycle in HeLa cells. *J. Cell Biol.* 74:468–491.

21. Safiulina, D., V. Veksler, A. Zharkovsky, and A. Kaasik. 2005. Loss of mitochondrial membrane potential is associated with increase in mitochondrial volume: Physiological role in neurones. *J. Cell. Physiol.* 206:347–353.

22. Popov, V., N. I. Medvedev, H. A. Davies, and M. G. Stewart. 2005. Mitochondria form a filamentous reticular network in hippocampal dendrites but are present as discrete bodies in axons: a three-dimensional ultrastructural study. *J. Comp. Neurol.* 492:50–65.

23. Barsoum, M. J., H. Yuan, A. A. Gerencser, G. Liot, Y. Kushnareva, S. Graber, I. Kovacs, W. D. Lee, J. Waggoner, J. Cui, A. D. White, B. Bossy, J. C. Martinou, R. J. Youle, S. A. Lipton, M. H. Ellisman, G. A. Perkins, and E. Bossy-Wetzel. 2006. Nitric oxide-induced mitochondrial fission is regulated by dynamin-related GTPases in neurons. *EMBO J.* 25:3900–3911.

24. Quinlan, P. T., A. P. Thomas, A. E. Armston, and A. P. Halestrap. 1983. Measurement of the intramitochondrial volume in hepatocytes without cell disruption and its elevation by hormones and valinomycin. *Biochem. J.* 214:395–404.

25. Das, M., J. E. Parker, and A. P. Halestrap. 2003. Matrix volume measurements challenge the existence of diazoxide/glibencamide-sensitive KATP channels in rat mitochondria. *J. Physiol.* 547:893–902.

26. Pfeiffer, D. R., T. I. Gudz, S. A. Novgorodov, and W. L. Erdahl. 1995. The peptide mastoparan is a potent facilitator of the mitochondrial permeability transition. *J. Biol. Chem.* 270:4923–4932.

27. He, L. H., and J. J. Lemasters. 2002. Regulated and unregulated mitochondrial permeability transition pores: a new paradigm of pore structure and function? *FEBS Lett.* 512:1–7.

28. Brustovetsky, N., T. Brustovetsky, R. Jemmerson, and J. M. Dubinsky. 2002. Calcium-induced cytochrome *c* release from CNS mitochondria is associated with the permeability transition and rupture of the outer membrane. *J. Neurochem.* 80:207–218.

29. Yuste, R., F. Lanni, and A. Konnerth. 2000. Imaging Neurons. Cold Spring Harbor Laboratory Press, Cold Spring Harbor, NY.

30. Nicholls, D. G. 2004. Mitochondrial dysfunction and glutamate excitotoxicity studied in primary neuronal cultures. *Curr. Mol. Med.* 4:149–177.

31. Johnson-Cadwell, L. I., M. B. Jekabsons, A. Wang, B. M. Polster, and D. G. Nicholls. 2007. ''Mild uncoupling'' does not decrease mitochondrial superoxide levels in cultured cerebellar granule neurons but decreases spare respiratory capacity and increases toxicity to glutamate and oxidative stress. *J. Neurochem.* 101:1619–1631.

32. Beavis, A. D., R. D. Brannan, and K. D. Garlid. 1985. Swelling and contraction of the mitochondrial matrix. I. A structural interpretation of the relationship between light scattering and matrix volume. *J. Biol. Chem.* 260:13424–13433.

33. Hackenbrock, C. R. 1966. Ultrastructural bases for metabolically linked mechanical activity in mitochondria. I. Reversible ultrastructural changes with change in metabolic steady state in isolated liver mitochondria. *J. Cell Biol.* 30:269–297.

34. Mannella, C. A., D. R. Pfeiffer, P. C. Bradshaw, I. I. Moraru, B. Slepchenko, L. M. Loew, C. E. Hsieh, K. Buttle, and M. Marko. 2001. Topology of the mitochondrial inner membrane: dynamics and bioenergetic implications. *IUBMB Life*. 52:93–100.

35. Doran, E., and A. P. Halestrap. 2000. Cytochrome *c* release from isolated rat liver mitochondria can occur independently of outer-membrane rupture: possible role of contact sites. *Biochem. J.* 348:343–350.

36. Andreyev, A. Y., B. Fahy, and G. Fiskum. 1998. Cytochrome *c* release from brain mitochondria is independent of the mitochondrial permeability transition. *FEBS Lett.* 439:373–376.

37. Loew, L. M., R. A. Tuft, W. Carrington, and F. S. Fay. 1993. Imaging in five dimensions: time-dependent membrane potentials in individual mitochondria. *Biophys. J.* 65:2396–2407.

38. Webb, R. 1996. Confocal optical microscopy. *Rep. Prog. Phys.* 59:427–471.

39. Pivovarova, N. B., H. V. Nguyen, C. A. Winters, C. A. Brantner, C. L. Smith, and S. B. Andrews. 2004. Excitotoxic calcium overload in a subpopulation of mitochondria triggers delayed death in hippocampal neurons. *J. Neurosci.* 24:5611–5622.

40. Gerencser, A. A., and V. Adam-Vizi. 2005. Mitochondrial Ca^{2+} dynamics reveals limited intramitochondrial Ca^{2+} diffusion. *Biophys. J.* 88:698–714.

41. Venerando, R., G. Miotto, P. Pizzo, R. Rizzuto, and N. Siliprandi. 1996. Mitochondrial alterations induced by aspirin in rat hepatocytes expressing mitochondrially targeted green fluorescent protein (mtGFP). *FEBS Lett.* 382:256–260.

42. De Vos, K. J., V. J. Allan, A. J. Grierson, and M. P. Sheetz. 2005. Mitochondrial function and actin regulate dynamin-related protein 1-dependent mitochondrial fission. *Curr. Biol.* 15:678–683.

43. Smirnova, E., D. L. Shurland, S. N. Ryazantsev, and A. M. van der Bliek. 1998. A human dynamin-related protein controls the distribution of mitochondria. *J. Cell Biol.* 143:351–358.

44. Kaasik, A., D. Safiulina, V. Choubey, M. Kuum, A. Zharkovsky, and V. Veksler. 2007. Mitochondrial swelling impairs the transport of organelles in cerebellar granule neurons. *J. Biol. Chem.* 282:32821–32826.

45. Gunawardena, S., L. S. Her, R. G. Brusch, R. A. Laymon, I. R. Niesman, B. Gordesky-Gold, L. Sintasath, N. M. Bonini, and L. S. Goldstein. 2003. Disruption of axonal transport by loss of huntingtin or expression of pathogenic polyQ proteins in *Drosophila. Neuron.* 40:25–40.